Late inception of a resiliently oxygenated upper ocean

Wanyi Lu[1], Andy Ridgwell[2,3], Ellen Thomas[4,5], Dalton S. Hardisty[6], Genming Luo[7], Thomas J. Algeo[7,8,9], Matthew R. Saltzman[10], Benjamin C. Gill[11], Yanan Shen[12], Hong-Fei Ling[13], Cole T. Edwards[14], Michael T. Whalen[15], Xiaoli Zhou[1], Kristina M. Gutchess[1], Li Jin[16], Rosalind E. M. Rickaby[17], Hugh C. Jenkyns[17], Timothy W. Lyons[2], Timothy M. Lenton[18], Lee R. Kump[19] and Zunli Lu[1*]

1 Department of Earth Sciences, Syracuse University, Syracuse, NY, USA
2 Department of Earth Sciences, University of California, Riverside, CA, USA
3 School of Geographical Sciences, University of Bristol, Bristol, UK
4 Department of Geology and Geophysics, Yale University, New Haven, CT, USA,
5 Department of Earth and Environmental Sciences, Wesleyan University, Middletown, CT, USA
6 Department of Earth and Environmental Sciences, Michigan State University, East Lansing, MI, USA
7 State Key Laboratory of Biogeology and Environmental Geology and School of Earth Science, China University of Geosciences, Wuhan, China
8 State Key Laboratory of Geological Processes and Mineral Resources, China University of Geosciences, Wuhan, China
9 Department of Geology, University of Cincinnati, Cincinnati, OH, USA
10 School of Earth Sciences, The Ohio State University, Columbus, OH, USA
11 Department of Geosciences, Virginia Polytechnic and State University, Blacksburg, VA, USA
12 School of Earth and Space Sciences, University of Science and Technology of China, Hefei, China
13 State Key Laboratory for Mineral Deposits Research, School of Earth Sciences and Engineering, Nanjing University, Nanjing, China
14 Department of Geological and Environmental Sciences, Appalachian State University, Boone, NC, USA
15 Department of Geosciences, University of Alaska Fairbanks, Fairbanks, AK, USA
16 Geology Department, State University of New York College at Cortland, Cortland, NY, USA
17 Department of Earth Sciences, University of Oxford, Oxford, UK
18 Earth System Science group, College of Life and Environmental Sciences, University of Exeter, Exeter, UK
19 Department of Geosciences, Pennsylvania State University, University Park, PA, USA

* Email: zunlilu@syr.edu

Rising oceanic and atmospheric oxygen levels through time have been crucial to enhanced habitability of surface Earth environments. Few redox proxies can track secular variations in dissolved oxygen concentrations ($[O_2]$) around threshold levels for metazoan survival in the upper ocean. We present an extensive compilation of iodine to calcium ratios (I/Ca) in marine carbonates. Our record supports a major rise in atmospheric pO_2 at ~400 million years ago (Ma), and reveals a step-change in the oxygenation of the upper ocean to relatively sustainable near-modern conditions at ~200 Ma. An Earth system model demonstrates that a shift in organic matter remineralization to greater depths, which may have been due to increasing size and biomineralization of eukaryotic plankton, likely drove the I/Ca signals at ~200 Ma.

The evolution and survival of marine animals depends on oxygen availability, particularly in upper ocean waters – ranging from the sea surface to the thermocline – during early Earth history (*1*). The $[O_2]$ in the upper ocean commonly decreases from the well-mixed surface ocean (top few tens of meters) into deeper subsurface waters (a few hundred meters). This $[O_2]$ gradient is controlled by three key factors: (i) the partial pressure of oxygen in the atmosphere (pO_2), (ii) the intensity of upper ocean mixing and (iii) oxidation of organic matter in the water column which consumes oxygen (*2*). Atmospheric pO_2 changes through time have been estimated via geochemical proxy data and box models (*3*). Oceanic

paleo-redox proxies typically track the areal extent of euxinic waters (containing H_2S) and the presence/absence of anoxia (positive/zero $[O_2]$) (*4, 5*). Since most modern marine animals are sensitive to $[O_2]$ changes between ~10 and ~100 μmol/kg (*2*), development of long-term proxy reconstructions for $[O_2]$ in this critical range (oxic–hypoxic) would help elucidate when and how oceanic oxygenation evolved to accommodate the modern ecological landscape.

Carbonate I/Ca is one of the novel proxies developed for the oxic–hypoxic window with the potential to reconstruct secular trends in upper-ocean oxygenation (*6, 7*). The long residence time of iodine (~300 kyr) leads to generally uniform total iodine concentrations in the modern ocean, but speciation changes of iodine between iodate (IO_3^-) and iodide (I^-) are controlled locally (*8, 9*). IO_3^- is completely reduced to I^- in waters at low $[O_2]$ (*8, 9*) and re-oxidized under well-oxygenated conditions. Since IO_3^- is the only chemical form of iodine incorporated into the carbonate structure (*7*) by replacing the CO_3^{2-} ion (*10*), carbonate I/Ca records of local seawater $[IO_3^-]$ through time can indicate changes in $[O_2]$. Carbonate I/Ca has been shown to be a reliable tracer responding primarily to $[O_2]$ variations in marine environments over a wide range of geological periods (*6, 11-16*).

We measured I/Ca in an extensive Phanerozoic collection of shallow marine carbonates likely forming within the top 200 m of the water column and compiled them with published data (Table S1 and Fig. 1A). Maximum I/Ca values for individual localities were generally low in the Proterozoic, except for periods which have been associated with potential atmospheric pO_2 rises [e.g., the Great Oxidation Event (*12*) and some Neoproterozoic carbon isotope excursions (*11, 15*), when maximum values temporarily increased to Cenozoic levels (3–4 μmol/mol) (Fig. 1A). Paleozoic maximum values are comparable to those of the Proterozoic, despite a relatively short spike during the Devonian, at approximately 400 Ma, when the 75th percentile values reached Cenozoic levels. Break point analyses indicate a step-change at Triassic to early Jurassic (~200 Ma, Fig. S1), after which maximum values remain above 4 μmol/mol and 75th percentile values are mostly higher than 3 μmol/mol (*6, 13*). The Devonian I/Ca excursion and the step-change at ~ 200 Ma are two key observations in this data compilation.

The stark contrast between predominantly low Paleozoic values and high Meso-Cenozoic values (excluding the Triassic, i.e., <200 Ma) cannot be explained by sampling biases. The sample size for the Paleozoic (n = 894) is comparable to that for the Proterozoic (n = 1078) and the Meso-Cenozoic (n = 926). The sampling density (number of samples per unit time) is similar in the Paleozoic and Meso-Cenozoic, although lower in the Proterozoic (Fig. 1B). For Paleozoic samples, we targeted carbonate- and fossil-rich (shallow) continental-shelf locations, i.e., relatively well-oxygenated settings, which are prone to record high I/Ca values. By contrast, many Mesozoic data were generated from sections recording well-established global oceanic anoxic events (OAEs), which, if anything, would bias that dataset toward low values. Cenozoic I/Ca values were measured in sediment coarse fraction, which may better preserve primary I/Ca signatures than bulk-rock samples. Existing early Cenozoic (*14*) and Cretaceous I/Ca data (*13*) are generally comparable across different lithologies, although comparisons between the Cenozoic and other periods are more tenuous. The current data set has relatively denser sample coverage for intervals coinciding with Earth-system perturbations (e.g., major carbon-isotope excursions and mass extinctions) than for extended intervals with limited environmental changes, but this should not influence main features of the data compilation.

I/Ca values can potentially be reduced during subaerial exposure, marine burial and dolomitization, but no post-depositional alterations are known to increase I/Ca (*11*). A variety of diagenesis indicators were considered in previous studies of samples that we used here (*7, 15-17*). In all of those case studies, the number of potentially altered samples was limited and did not influence the

central trend of the majority of the data through time, as represented by the 25th and 75th percentile values (Fig. 1A). High I/Ca values throughout the record (Fig. 1A) are not consistently tied to a specific inferred primary carbonate mineralogy (e.g., calcite *vs* aragonite seas, Fig. S2A). The distinct behaviors of I/Ca before and after ~200 Ma (Fig. 1A) cannot be explained by secular changes in seawater [Ca^{2+}] (Fig. S2B). No evidence suggests that differences in Paleozoic and Mesozoic I/Ca distributions were due to uniformly greater alteration of the Paleozoic samples (Fig. S3). Lower relative standard deviations (RSD) of neighboring samples in each section (i.e., smoother I/Ca profiles; Fig. S4) may reflect better preservation of the Paleozoic than the Proterozoic samples (Fig. S4).

We interpret I/Ca in marine carbonates primarily as a qualitative indicator for the depth of the oxycline (Fig. 2), i.e., that part of water column where the [O_2] decreases relatively abruptly. Carbonate rocks formed in the upper ocean record surface or near-surface seawater [IO_3^-], which is strongly affected by the presence/absence of a proximal oxygen minimum zone (OMZ) or a shallow oxycline. Due to the relatively slow oxidation kinetics of I^- (*18*), surface waters may retain a low iodate signal despite high *in situ* [O_2] levels. For instance, core-top (modern) planktonic foraminiferal shells exhibit low I/Ca values (~0.5 μmol/mol) in waters above a shallow OMZ in the equatorial Pacific, but record higher values (>3 μmol/mol) at other well-oxygenated locations (*6*).

The large I/Ca excursion during the Devonian (Fig. 3) most likely reflects deepening of the oxycline and development of better oxygenated conditions in the upper ocean, consistent with published proxy data and modeling results (*4, 5, 19, 20*). Although different box models yield somewhat divergent interpretations of atmospheric pO_2 variation through the Phanerozoic (*21-24*), a Devonian rise in pO_2 levels is plausible, based on the COPSE model and charcoal proxy reconstructions (Fig. 3A), and was most likely due to increased abundance of vascular land plants (*19, 20*). Previous work interpreted δ^{98}Mo, iron-speciation and biological data (Fig. 3C) to reflect oceanic redox changes, supporting the idea of atmospheric pO_2 rise during the Devonian (*4, 5*). The combination of these independent proxies indicates that the Devonian atmospheric pO_2 rise impacted the whole atmosphere-ocean system, across the entire redox spectrum (Fig. 3).

I/Ca values returned to Proterozoic-like levels following the transient Devonian excursion, but there is no evidence for a pO_2 decrease to pre-Devonian levels between the Carboniferous and the Triassic. Instead, the post-Devonian atmosphere was probably relatively O_2-rich (Fig. 3A). High atmospheric pO_2 likely altered terrestrial weathering feedbacks and enhanced nutrient delivery to the ocean (*25, 26*), leading to intensified O_2 consumption in the upper ocean, a generally shallow oxycline, and low I/Ca values between ~400 and 200 Ma (Fig. 3B). Under such conditions, carbonates formed in surface-oceans rapidly equilibrated with the high-pO_2 atmosphere would record low *in situ* [IO_3^-] due to the slow oxidation of I^- during mixing between surface and subsurface waters (Fig. 2B). If the oxycline were indeed shallow, marine animals on continental shelves at that time (~ 200-400 Ma) would have been living in a thin layer of well-oxygenated surface water directly underlain by an OMZ (Fig. 2B). Our dataset (Fig. 1A) implies that well-oxygenated upper-ocean conditions became persistent and resilient only by the Triassic-Jurassic (~200 Ma), much later than previously inferred (*27*). The prerequisites for achieving such well-oxygenated upper-ocean conditions are a combination of high atmospheric pO_2 and a generally deep oxycline (Fig. 2C). The position of the oxycline is strongly controlled by the depth of organic-matter remineralization, which is dependent on the efficiency of organic-matter export from the photic zone, and has been proposed as a governing parameter for OMZs during the Phanerozoic (*28*).

We hypothesize that changes in remineralization of organic matter strongly influenced the upper-ocean I/Ca signature (Fig. 2), and we tested this hypothesis by simulating the marine iodine cycle in the 'cGENIE' Earth system model (see Methods, Fig. S5) (*29*). We aimed to identify possible causes for low

I/Ca during the Paleozoic through ensembles of model runs using a range of values for atmospheric pO_2, the depth of organic-matter remineralization in the water column, and the mean concentrations of iodine and phosphate in seawater. For each Paleozoic model run, surface-water [IO_3^-] values along continental margins were extracted to calculate a relative frequency distribution (Fig. S6). The modeled IO_3^- distributions were compared with observed Paleozoic I/Ca distributions (Fig. 1C) to obtain the residual sum of squares (RSS) (see Materials and Methods, Fig. 4A and Fig. S7).

We found that the lowest RSS values (<0.05), representing the best data-model fits, were achieved at shallow remineralization depths [i.e., <0.5 present oceanic level (POL)]. In the same set of cGENIE runs (Fig. 4B), lower RSS values correlated with lower average [O_2] in the subsurface layer (80-176 m), which is consistent with a shallower oxycline. Even as Paleozoic oceans experienced transitions between greenhouse and icehouse climate conditions, pCO_2 levels appear to have had minimal influence on IO_3^- distributions (Fig. S8). Global-scale changes in ocean circulation and continent configuration also do not significantly influence the oxycline depths independently of pO_2 and subsurface oxygen consumption (Fig. S9). The RSS contours differed only slightly when the Paleozoic I/Ca distribution was compared with modeled [IO_3^-] distributions in the top four layers in the upper ocean (from 0 to 410 m, Fig. S10). Thus, a lack of precise constraints on the paleo-depths of carbonate formation is unlikely to have affected the main conclusions of our data–model comparison. Additional model runs also suggest that oceanic nutrient levels and total iodine concentrations are unlikely to dominate the secular trends in proxy data (Fig. S11-12). Our data-model comparison (Fig. 4A) should not be viewed as a precise estimate of the atmospheric pO_2 for any single time slice, since the data were compiled over the entire Paleozoic under varying pO_2 levels. Thus, the lower RSS values at pO_2 below 1 PAL suggest that some portions of the Paleozoic may have had pO_2 levels lower than today (*5, 23*).

Based on our data compilation and model analyses, we attribute the transition at ~200 Ma from Proterozoic-like low I/Ca values in the Paleozoic (except for the mid-Devonian) to modern-like high values in the Meso-Cenozoic, to a profound increase in the average remineralization depth of organic matter in the water column. The timing of this transition is consistent with the proliferation of eukaryotic phyto- and zooplankton after the Permian-Triassic extinction (Fig. 3A)(*30, 31*), which eventually shaped the ecological landscape of the modern ocean (*32*). The larger size of primary producers (*33*), grazing/repackaging of organic matter into fecal pellets (*34*), and/or the advent of mineralized plankton (*32*) may have led to faster sinking of organic matter, which reduced O_2 utilization in the upper water column and caused a pervasive deepening of the oxycline (*28*).

The rise of oxygen levels over geological time has been linked to increases in animal body size (*24, 35*). A comprehensive compilation of Phanerozoic marine animal body-size data (*36*) shows that maximum bio-volume probably co-varied with I/Ca to some extent (Fig. 3B), indicating that O_2 availability in the global upper ocean may have been an important factor in Phanerozoic metazoan evolution. New forms of organisms (e.g., mineralized plankton, larger animals) fundamentally influenced oceanic environments, which in turn affected the evolving biosphere, representing a prime example of the co-evolution of life and planet.

Figure captions

Figure 1. Carbonate I/Ca through time. A. Candlestick plot showing ranges of I/Ca values for Proterozoic (red)(*11, 15*), Paleozoic (blue) and Meso-Cenozoic (purple). Boxes mark the 25th and 75th percentiles of values at each locality, and the whiskers show the maximum and minimum. Note that the Proterozoic values from dolostones are I/(Mg+Ca). **B.** Number of samples measured at each section. **C.** Relative frequency distributions of I/Ca.

Figure 2. Schematic illustrations for the evolution of oxygenation conditions. These simplified cartoons are not intended to capture all temporal and spatial variations.

Figure 3. Phanerozoic I/Ca compared with atmospheric pO_2, oceanic oxygenation and animal evolution trends. A. Modeled atmospheric pO_2 curves (*5, 21, 23, 24*) in comparison with the charcoal proxy record (*20*). Dashed lines (*5*) mark a broadly defined ocean-atmospheric O_2 level, not just atmospheric pO_2. **B.** I/Ca records through Phanerozoic. Blue boxes for bulk carbonate rock, gray boxes for bulk coarse fraction of Ocean Drilling Project samples (>63 μm). **C**. Marine animal body size record (*36*). Thickness of green bars indicates relative generic diversity modified from literature (*31, 32*). The red *vs* blue bars mark greenhouse *vs* icehouse climate conditions, respectively.

Figure 4. Residual sum of squares (RSS) and subsurface [O_2] at different pO_2 levels and remineralization depths. A. Shallow remineralization depths (POL for present oceanic level) produce the best model fit (the smallest RSS < 0.05) to Paleozoic I/Ca distribution, at 1× CO_2 condition. White dots represent 45 cGENIE simulations defining the contours. **B.** Averaged [O_2] in the shallowest subsurface layer in each cGENIE run as an indicator of oxycline depth correlating with the RSS.

REFERENCES AND NOTES

1. A. H. Knoll, *Cold Spring Harbor Perspectives in Biology* **6**, (2014).
2. R. F. Keeling, A. Kortzinger, N. Gruber, *Annual Review of Marine Science* **2**, 199-229 (2010).
3. T. W. Lyons, C. T. Reinhard, N. J. Planavsky, *Nature* **506**, 307-315 (2014).
4. T. W. Dahl *et al.*, *PNAS* **107**, 17911-17915 (2010).
5. E. A. Sperling *et al.*, *Nature* **523**, 451-454 (2015).
6. Z. Lu *et al.*, *Nature Communications* **7:11146**, (2016).
7. Z. Lu, H. C. Jenkyns, R. E. M. Rickaby, *Geology* **38**, 1107–1110 (2010).
8. G. W. Luther, T. Campbell, *Deep-Sea Research Part A-Oceanographic Research Papers* **38**, S875-S882 (1991).
9. E. L. Rue, G. J. Smith, G. A. Cutter, K. W. Bruland, *Deep-Sea Research Part I-Oceanographic Research Papers* **44**, 113-134 (1997).
10. J. Podder *et al.*, *Geochim. Cosmochim. Acta* **198**, 218-228 (2017).
11. D. S. Hardisty *et al.*, *Earth Planet. Sci. Lett.* **463**, 159-170 (2017).
12. D. S. Hardisty *et al.*, *Geology*, (2014).
13. X. Zhou *et al.*, *Paleoceanography* **30**, 510-526 (2015).
14. X. L. Zhou, E. Thomas, R. E. M. Rickaby, A. M. E. Winguth, Z. L. Lu, *Paleoceanography* **29**, 964-975 (2014).
15. W. Lu *et al.*, *Geochemical Perspectives Letters* **5**, 53-57 (2017).
16. C. T. Edwards, D. A. Fike, M. R. Saltzman, W. Lu, Z. Lu, *Earth Planet. Sci. Lett.* **481**, 125-135 (2018).
17. G. R. Loope, L. R. Kump, M. A. Arthur, *Chem. Geol.* **351**, 195-208 (2013).
18. R. Chance, A. R. Baker, L. Carpenter, T. D. Jickells, *Environmental Science-Processes & Impacts* **16**, 1841-1859 (2014).
19. T. M. Lenton *et al.*, *Proceedings of the National Academy of Sciences* **113**, 9704-9709 (2016).
20. I. J. Glasspool, A. C. Scott, *Nat. Geosci.* **3**, 627-630 (2010).
21. R. A. Berner, *Geochim. Cosmochim. Acta* **70**, 5653-5664 (2006).
22. N. M. Bergman, T. M. Lenton, A. J. Watson, *Am. J. Sci.* **304**, 397-437 (2004).
23. T. M. Lenton, S. J. Dainesa, B. J. Mills, *Earth Sci Rev* **178**, 1-28 (2018).
24. P. G. Falkowski *et al.*, *Science* **309**, 2202-2204 (2005).
25. L. R. Kump, *Nature* **335**, 152-154 (1988).
26. T. J. Algeo, R. A. Berner, J. B. Maynard, S. E. Scheckler, *GSA Today* **5**, 64–66 (1995).
27. H. D. Holland, *Philosophical Transactions of the Royal Society B-Biological Sciences* **361**, 903-915 (2006).
28. K. M. Meyer, A. Ridgwell, J. L. Payne, *Geobiology* **14**, 207-219 (2016).
29. A. Ridgwell *et al.*, *Biogeosciences* **4**, 87-104 (2007).
30. M. E. Katz, Z. V. Finkel, D. Grzebyk, A. H. Knoll, P. G. Falkowski, *Annual Review of Ecology Evolution and Systematics* **35**, 523-556 (2004).
31. R. E. Martin, *Global Planet. Change* **11**, 1-23 (1995).
32. P. G. Falkowski *et al.*, *Science* **305**, 354-360 (2004).
33. N. J. Butterfield, *Geobiology* **7**, 1-7 (2009).
34. G. A. Logan, J. M. Hayes, G. B. Hieshima, R. E. Summons, *Nature* **376**, 53-56 (1995).
35. J. L. Payne *et al.*, *Photosynth. Res.* **107**, 37-57 (2011).
36. N. A. Heim, M. L. Knope, E. K. Schaal, S. C. Wang, J. L. Payne, *Science* **347**, 867-870 (2015).
37. L. Cao *et al.*, *Biogeosciences* **6**, 375-390 (2009).
38. A. Tagliabue *et al.*, *Global Biogeochem. Cycles* **30**, 149-174 (2016).
39. H. Elderfield, V. W. Truesdale, *Earth Planet. Sci. Lett.* **50**, 105-114 (1980).
40. S. K. Lyons *et al.*, *Nature* **529**, 80-U183 (2016).
41. L. A. Hardie, *Geology* **31**, 785-788 (2003).
42. J. Farkas *et al.*, *Geochim. Cosmochim. Acta* **71**, 5117-5134 (2007).

43. A. Ridgwell, *Mar. Geol.* **217**, 339-357 (2005).
44. T. K. Lowenstein, L. A. Hardie, M. N. Timofeeff, R. V. Demicco, *Geology* **31**, 857-860 (2003).
45. R. A. Berner, *Am. J. Sci.* **304**, 438-453 (2004).
46. L. A. Hardie, *Geology* **24**, 279-283 (1996).
47. A. Ridgwell, D. N. Schmidt, *Nat. Geosci.* **3**, 196-200 (2010).
48. A. Schmidt *et al.*, *Nat. Geosci.* **9**, 77-+ (2016).
49. F. M. Monteiro, R. D. Pancost, A. Ridgwell, Y. Donnadieu, *Paleoceanography* **27**, (2012).
50. B. Kendall *et al.*, *Geochim. Cosmochim. Acta* **156**, 173-193 (2015).
51. X. Zhou *et al.*, *Chem. Geol.* **457**, 95-106 (2017).

ACKNOWLEDGEMENTS:

Funding: We thank NSF EAR-1349252, OCE-1232620, OCE-1736542 (Z.L.); NERC NE/J01043X/1, ERC-2013-CoG-617313, NSF OCE-1736771 (A.R.); NSF OCE-1736538 (E.T.); National Key R&D Project of China (2016YFA0601104) and NSFC 41290260 (G.L.); CAS (QYZDY-SSW-DQC031) and the "111" project (Y.S.); Wolfson Research Merit award from the Royal Society and EU award (R.E.M.R.); NERC NE/N018508/1, NE/P013643/1 (T.M.L.). **Author contributions:** Z.L. conceived the study. W.L. and Z.L. carried out the data analysis, model simulations and wrote the paper. A.R. modified cGENIE to incorporate iodine cycle. All authors contributed to data interpretation and the writing of the manuscript. **Competing interests:** The authors declare that they have no competing interests. **Data and materials availability:** all I/Ca data are available in the supplementary materials and online from https://www.pangaea.de/.

SUPPLEMENTARY MATERIALS

Materials and Methods
Figures S1 to S12
Captions for Tables S1 and S2
References (*37-51*)
Tables S1 and S2

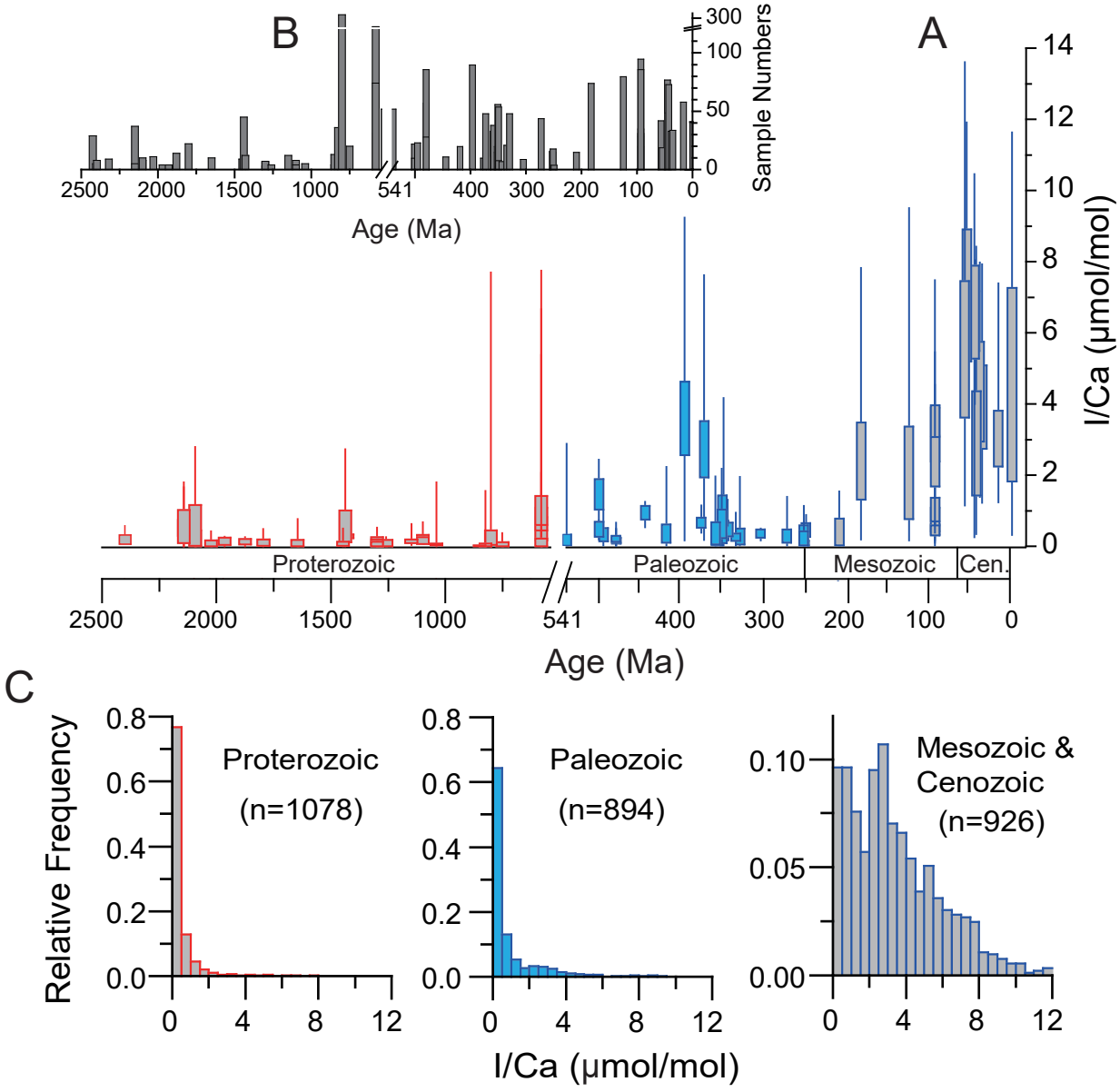
B
A
C
Sample Numbers
300
100
50
0
2500
2000
1500
1000
541
400
300
200
100
0
Age (Ma)
14
12
10
8
6
4
2
0
I/Ca (µmol/mol)
Proterozoic
Paleozoic
Mesozoic
Cen.
Relative Frequency
0.8
0.6
0.4
0.2
0.0
Proterozoic
(n=1078)
Paleozoic
(n=894)
0.10
0.05
0.00
Mesozoic &
Cenozoic
(n=926)
0
4
8
12
I/Ca (µmol/mol)

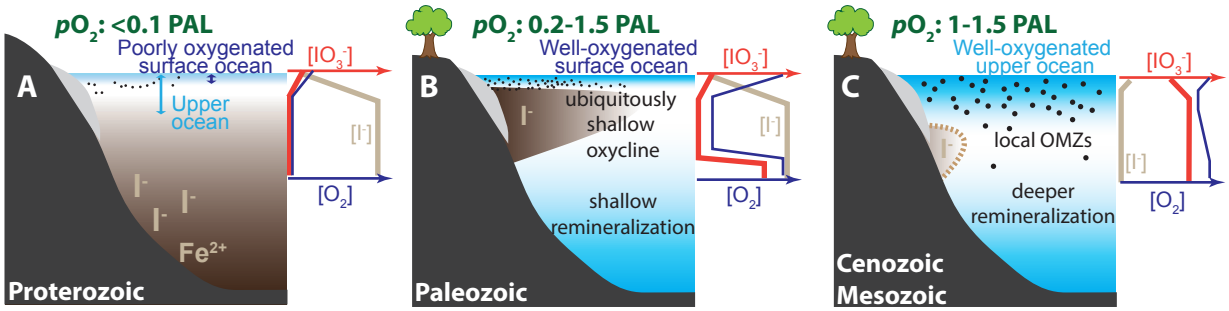
pO2: <0.1 PAL
Poorly oxygenated surface ocean
A
Upper ocean
I-
I-
I-
Fe2+
Proterozoic
[IO3-]
[I-]
[O2]
pO2: 0.2-1.5 PAL
Well-oxygenated surface ocean
B
I-
ubiquitously shallow oxycline
shallow remineralization
Paleozoic
[IO3-]
[I-]
[O2]
pO2: 1-1.5 PAL
Well-oxygenated upper ocean
C
I-
local OMZs
deeper remineralization
Cenozoic
Mesozoic
[IO3-]
[I-]
[O2]

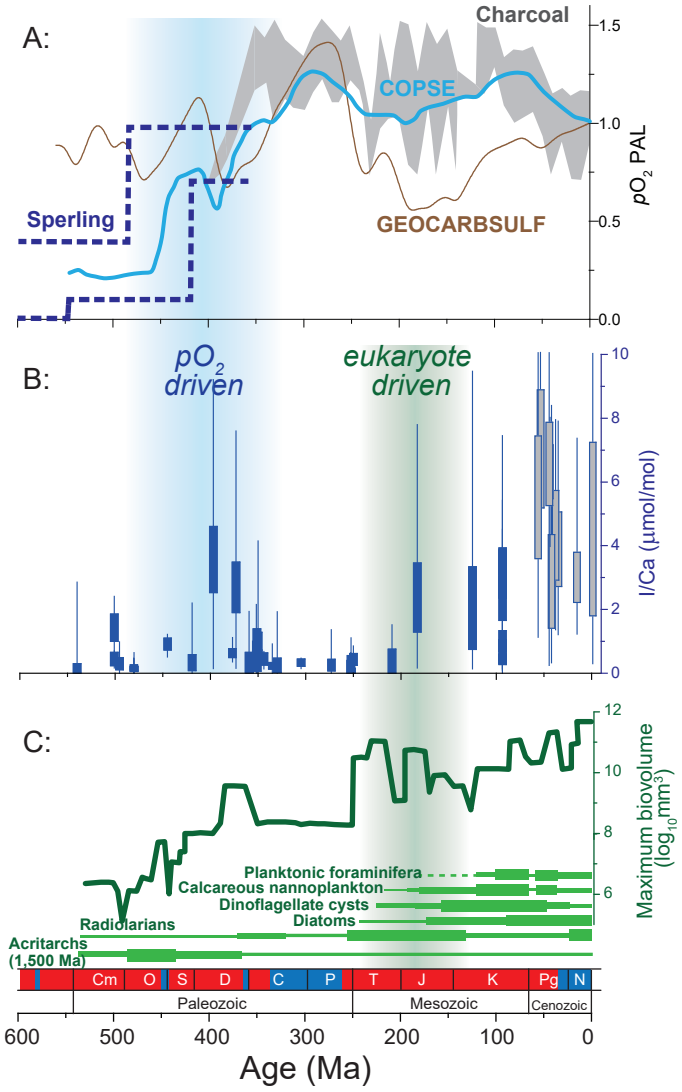
A:
Charcoal
COPSE
Sperling
GEOCARBSULF
pO2 PAL
1.5
1.0
0.5
0.0
B:
pO2 driven
eukaryote driven
I/Ca (µmol/mol)
10
8
6
4
2
0
C:
Maximum biovolume (log10mm3)
12
10
8
6
Planktonic foraminifera
Calcareous nannoplankton
Dinoflagellate cysts
Diatoms
Radiolarians
Acritarchs (1,500 Ma)
Cm
O
S
D
C
P
T
J
K
Pg
N
Paleozoic
Mesozoic
Cenozoic
600
500
400
300
200
100
0
Age (Ma)

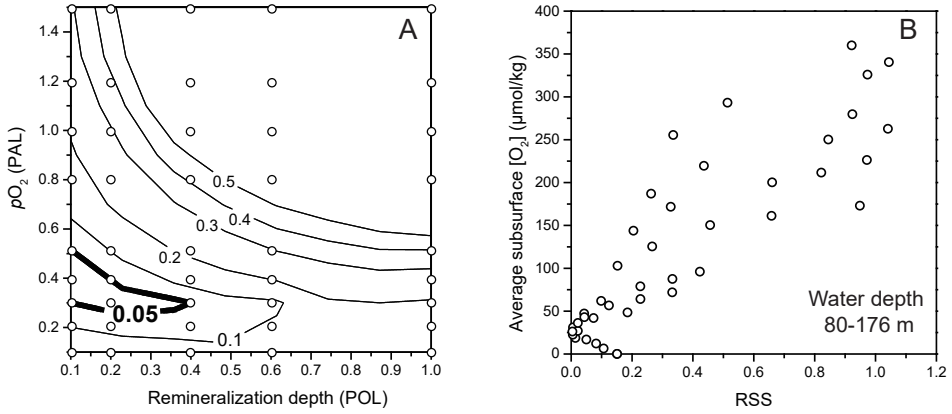
A
B
pO_2 (PAL)
Remineralization depth (POL)
0.05
0.1
0.2
0.3
0.4
0.5
Average subsurface [O_2] (µmol/kg)
RSS
Water depth
80-176 m

Supplementary Materials for

Late inception of a resiliently oxygenated upper ocean

Wanyi Lu, Andy Ridgwell, Ellen Thomas, Dalton S. Hardisty, Genming Luo, Thomas J. Algeo, Matthew R. Saltzman, Benjamin C. Gill, Yanan Shen, Hong-Fei Ling, Cole T. Edwards, Michael T. Whalen, Xiaoli Zhou, Kristina M. Gutchess, Li Jin, Rosalind E. M. Rickaby, Hugh C. Jenkyns, Timothy W. Lyons, Timothy M. Lenton, Lee R. Kump and Zunli Lu*.

correspondence to: zunlilu@syr.edu

This PDF file includes:

Other Supplementary Materials for this manuscript include the following:

Table S1 (.doc file)
Table S2 (.xlsx file)

Materials and Methods

I/Ca analyses

Bulk carbonate samples were crushed and homogenized to fine powder. Cenozoic sediment samples were wet sieved at 63 μm to obtain coarse-fraction samples (mostly foraminiferal tests), then crushed to powder. About 4 mg of powder from each sample were weighed and thoroughly rinsed with de-ionized water. 3% nitric acid was added for carbonate dissolution, and 0.1% tertiary amine solution was added to stabilize iodine. Iodine and calcium concentrations were then measured on a quadrupole inductively coupled plasma-mass spectrometer (ICP-MS) at Syracuse University. Iodine calibration standards were prepared daily from KIO_3 powder. The sensitivity of iodine was tuned to ~80 kcps for a 1 ppb standard. The precision for ^{127}I is normally better than 1%. The reference material JCp-1 was measured repeatedly to maintain long-term accuracy. The detection limit of I/Ca is approximately 0.1 μmol/mol.

Earth system modeling

We employ the 'cGENIE' Earth system model comprising a 3-D dynamic ocean circulation model with simplified energy-moisture balance atmosphere, and biogeochemical cycling of elements and isotopes in the ocean (*29*). This model has been extensively evaluated against modern observations of nutrients, oxygen, and carbon (*29, 37, 38*). We introduced new tracers for dissolved IO_3^- and I^-, iodine associated with particulate organic matter, and a set of transformations between them. We simulated four steps in iodine cycling in the water column that are most relevant to I/Ca. (1) Iodate is taken up by export production from surface water with a fixed iodine to organic carbon (I:C) 'Redfield'-like ratio (*39*). (2) In the reverse process – the remineralization of organic matter back to dissolved constituents – we release iodine back into solution in the form of iodide. (3) In subsurface waters, when $[O_2]$ falls below a specified threshold, IO_3^- is reduced to I^-. (4) Finally, we parameterize the oxidation of iodide to iodate according to a prescribed lifetime. Some of these processes are associated with significant uncertainties, e.g. the lifetime of iodide in oxic seawater (*18*).

In a series of 10-kyr-long model runs to steady state, the iodine cycle was then calibrated to the modern sea-surface iodate distribution to determine the $[O_2]$ threshold for complete IO_3^- reduction and I^- oxidation kinetics (iodide lifetime) (Fig. S5). For this data-model comparison, we calculated the residual sum of square (RSS) as follows:

$$\mathrm{RSS} = \sum_{i=1}^{n} \left(F_i - \widehat{F_i}\right)^2$$

where F_i is the relative frequency of i^{th} bin of measured data, and $\widehat{F_i}$ is the corresponding relative frequency of i^{th} bin of cGENIE results. Modern sea-surface iodate data (*18*) are distributed in 21 bins beginning at 0 and ending at 1.05 with bin size of 0.05. These parameter settings were then applied to model Paleozoic scenarios, for which we adopted a published end-Permian configuration (*28*) to represent average Paleozoic conditions. For data–model comparisons in our paleo experiments, I/Ca data are distributed in 24 bins beginning at 0 and ending at 12 with bin size of 0.5. Model results for the Paleozoic only use surface-water $[IO_3^-]$ along continental margins (Fig. S6). For testing the paleo-environmental parameters, we allowed each ensemble to have 45 runs and two varying parameters. Preliminary experiments show that pO_2, remineralization depth, and $[PO_4]$ are the most important parameters for $[IO_3^-]$ distribution patterns and, hence, for I/Ca

ratios. Iodine inventory changes in the model do not produce [IO_3^-] distributions resembling the Paleozoic I/Ca distribution and were therefore not tested in an ensemble.

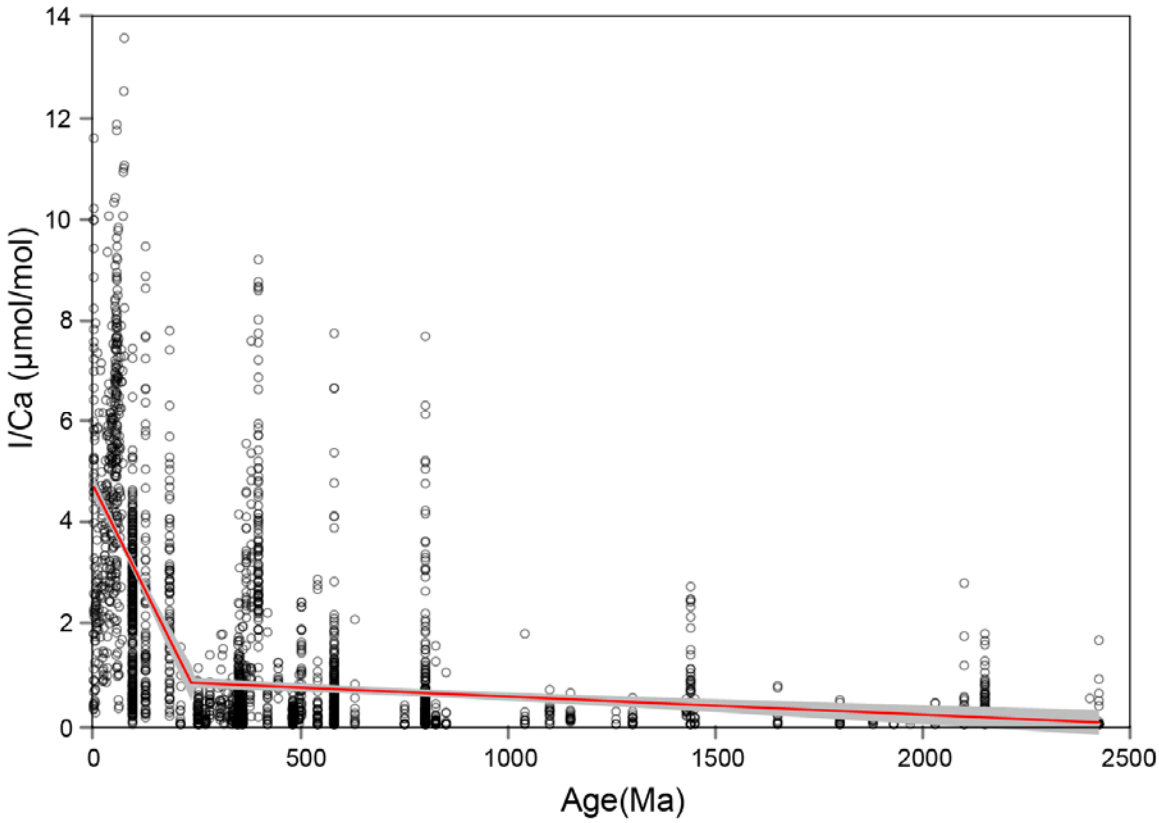

Fig. S1. Break point analyses (*40*). We used a maximum likelihood approach, via the R package 'segmented' version 1.4 to estimate the breakpoint time of I/Ca shift. Our analysis used an initial linear model of the I/Ca as a function of approximate sample age (Ma), to generate the best-fit number of breakpoints and fit separate regression lines to each segment. We performed a bootstrap of 1,000 replicates to estimate uncertainty in model parameters and age at which the breakpoint(s) occur. The result shows that the I/Ca shift began at 235 Ma. We further did a series of sensitivity tests by performing the same analysis while removing the data from a few different sections in each sensitivity test. The break point age could vary between 190 and 250 Ma, which suggest that we do not have sufficient data coverage to narrow down this age. Therefore, we refer to a generic number "~200 Ma" in the main text.

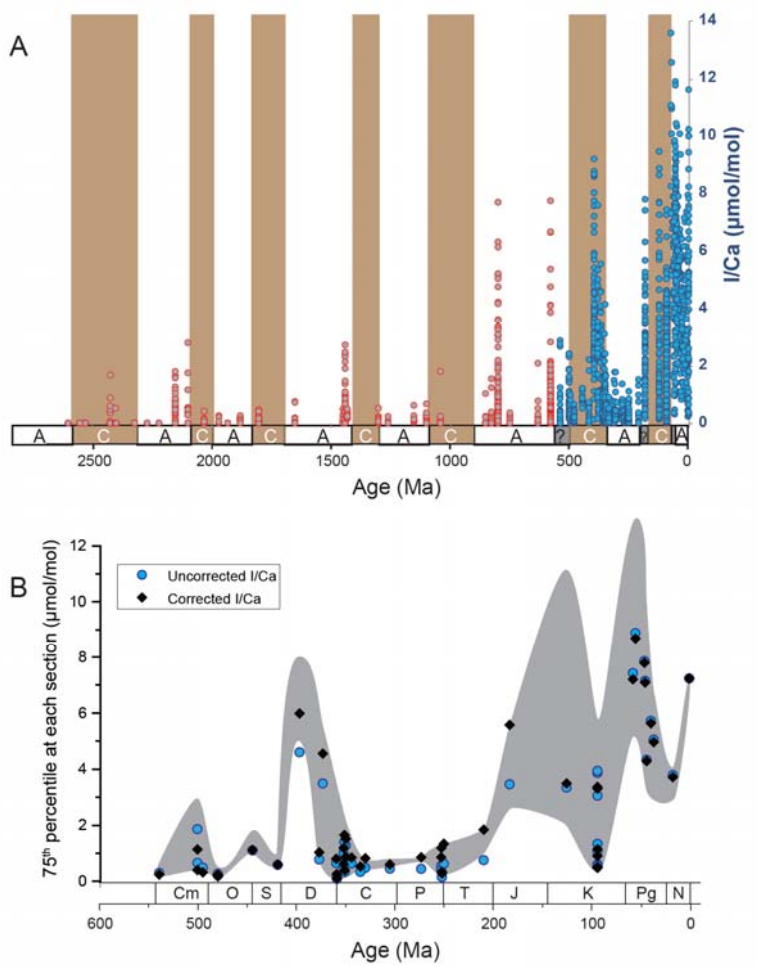

Fig. S2. A. I/Ca values in aragonite–calcite seas. No consistent association between high I/Ca values and carbonate mineralogy is observed ***(41)***. Proterozoic high I/Ca values were found more often in intervals characterized by aragonite seas, whereas the Phanerozoic high I/Ca values appear more frequently in intervals characterized by calcite seas. This pattern is the opposite of that predicted if diagenetic recrystallization of aragonite to calcite in reducing pore fluids were the main control on I/Ca through time. B. Secular changes in seawater $[Ca^{2+}]$ can influence carbonate I/Ca trends, in addition to oxygenation conditions. Iodate substitution in calcite (*10*) probably involves a double substitution, e.g. $IO_3^- + Na^+ \leftrightarrow Ca^{2+} + CO_3^{2-}$. Therefore, corrections to I/Ca should be based on $[Ca^{2+}]\times[CO_3^{2-}]$, instead of based on $[Ca^{2+}]$. Blue dots show the uncorrected 75th percentile values through the Phanerozoic, as in Figure 3B. Black diamonds show I/Ca corrected to modern seawater $[Ca^{2+}]\times[CO_3^{2-}]$ using Phanerozoic seawater $[Ca^{2+}]$ estimates derived from Ca-isotope data (*42*) and $[CO_3^{2-}]$ estimates from modeling (*43*). The gray band brackets the maximum and minimum of corrected 75th percentile values based on four different paleo-seawater $[Ca^{2+}]$ reconstructions (*42, 44-46*). Such corrections may improve the qualitative secular trend of I/Ca, but do not necessarily produce more reliable absolute values of I/Ca, because iodate substitution kinetics and partition coefficients may change in a non-linear fashion relative to $[Ca^{2+}]\times[CO_3^{2-}]$. Thus, this correction procedure can only qualitatively test first order impacts of seawater chemistry on the Phanerozoic I/Ca record.

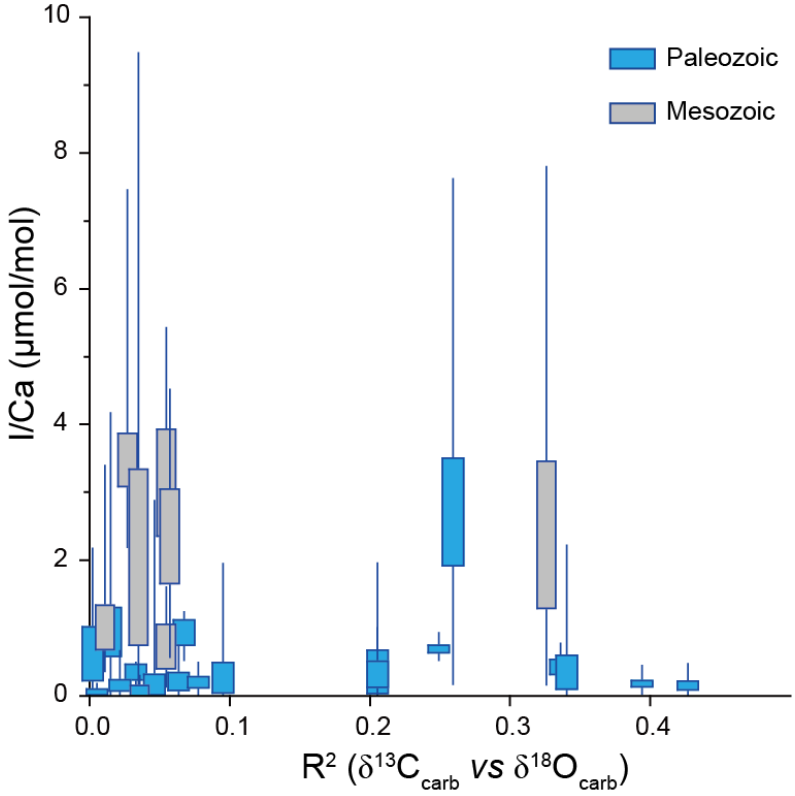

Fig. S3. R^2 of the correlation between $\delta^{13}C_{carb}$ and $\delta^{18}O_{carb}$ for each study section plotted against its range of I/Ca values. Higher R^2 indicate a greater possibility of diagenetic alteration. All known diagenetic alteration processes would decrease I/Ca ratios or have no effects. No evidence here indicates that the low I/Ca values of Paleozoic samples are due to significantly poorer preservation relative to Mesozoic samples.

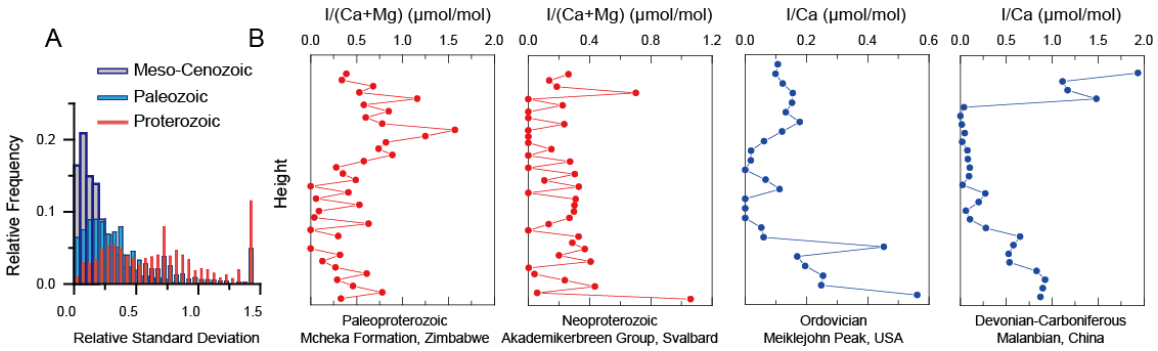

Fig. S4. A. Histograms for relative standard deviation (RSD) of I/Ca values in every three neighboring samples of each section. Low RSD values are much more frequently observed in the Paleozoic samples than in Proterozoic samples. **B**. Paleozoic profiles are often smoother than Proterozoic profiles, as shown in some examples for the low RSD values indicating better preservation in Paleozoic samples. Note that these selected profiles are used to demonstrate the source of low RSD values in Paleozoic samples, but not all Paleozoic profiles are smoother than all Proterozoic profiles. The lower RSDs of Mesozoic-Cenozoic samples compared to Paleozoic samples are likely due to higher absolute I/Ca values for Mesozoic-Cenozoic samples.

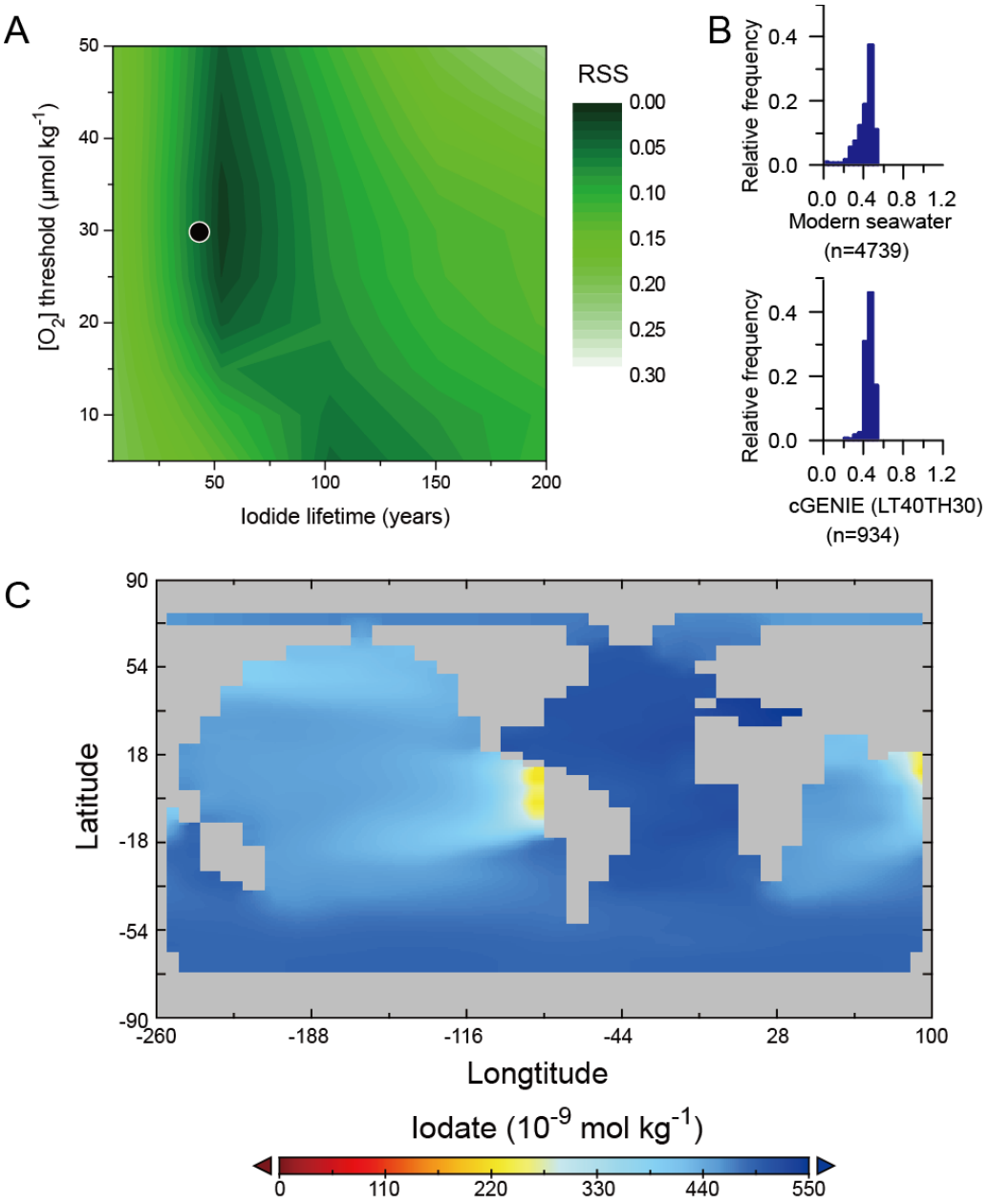

Fig. S5. A. Residual sum of squares (RSS) between cGENIE results and modern sea-surface iodate distributions to determine the [O_2] threshold for complete IO_3^- reduction to I^- and iodide lifetime. Simulations employed a modern configuration. The black circle represents the selection of iodide lifetime of 40 years and [O_2] threshold of 30 µmol/kg. These parameter values are used for all of the following model runs. Note that a lifetime of 50 years produced the lowest RSS, but the maximum lifetime in the literature is 40 years (*18*). Consequently, this value is adopted for Paleozoic model runs. **B.** Relative frequency distribution of modern sea-surface iodate (µM) (*18*) *vs* cGENIE results (40 years iodide lifetime and 30 µmol/kg [O_2] threshold). **C.** Surface-water iodate map simulated with these settings.

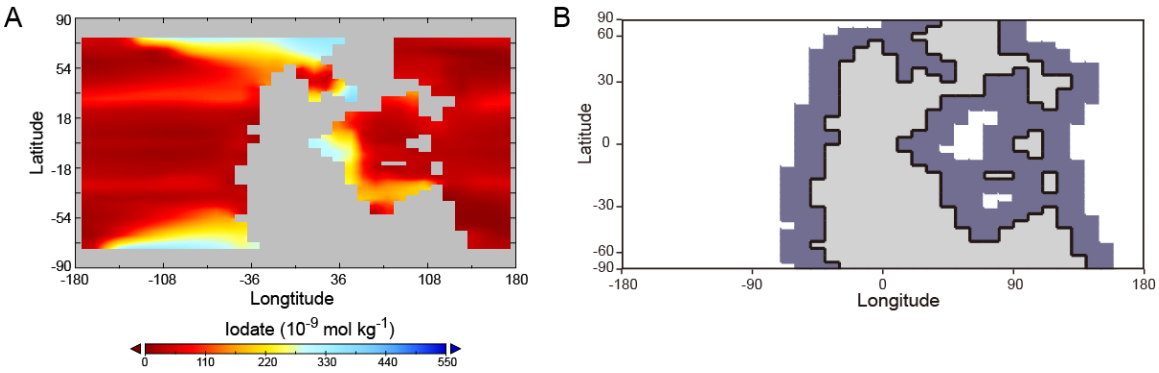

Fig. S6. A. Modeled surface-ocean [IO_3^-] map with the lowest RSS (0.01), which is the best fit to Paleozoic I/Ca data. The simulation employed an end-Permian geographic configuration, and 0.5× O_2, 8× CO_2, 0.1× remineralization depth, 1× [PO_4], 1× Total iodine, iodide lifetime of 40 years and 30 µmol/kg [O_2] threshold. **B.** All Paleozoic surface-ocean [IO_3^-] data generated within the purple shaded fields were treated as continental-margin locations. They were extracted to compute frequency distributions and RSS values.

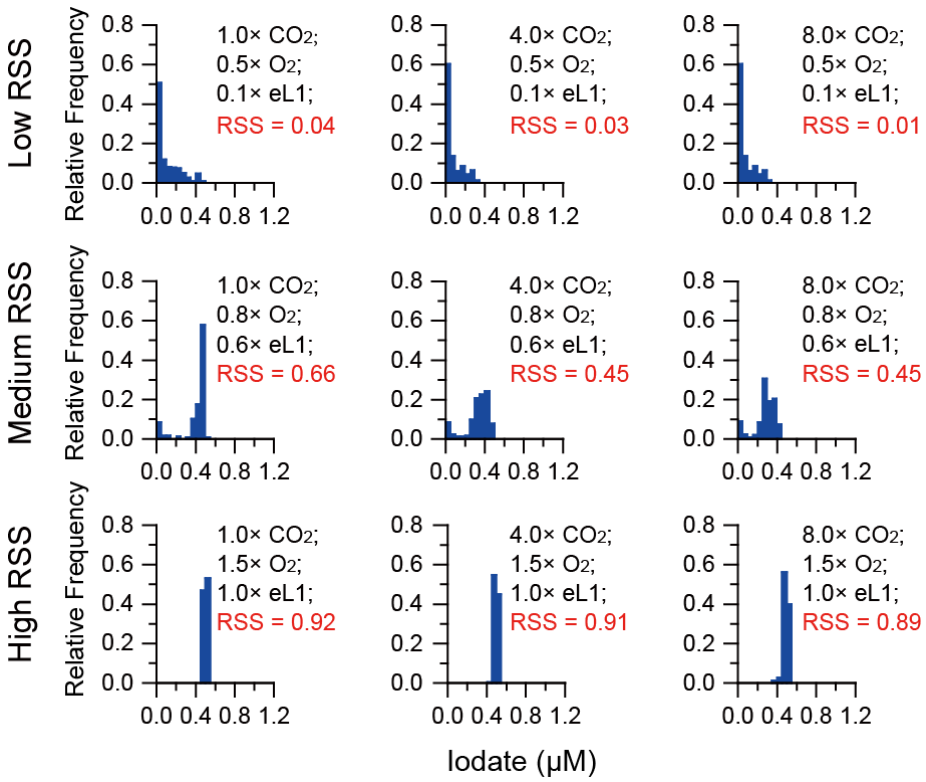

Fig. S7. Examples of modeled continental surface-ocean iodate histograms to illustrate low, medium, and high RSS values. All simulations employed an end-Permian geographic configuration, modern-level [PO_4] and total iodine, an iodide lifetime of 40 years, and a 30 μmol/kg [O_2] threshold. eL1 denotes remineralization depth.

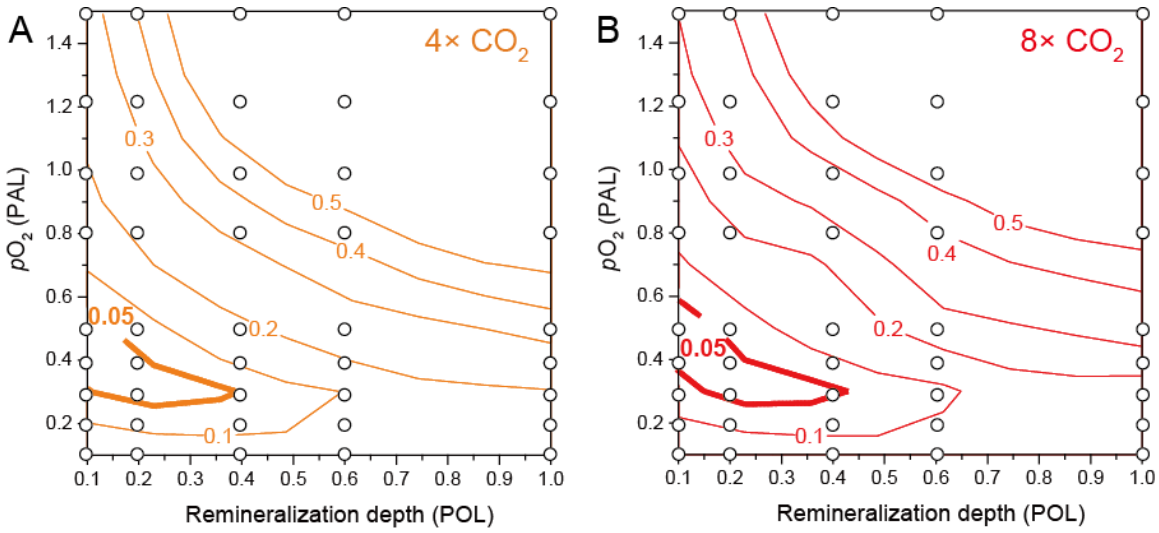

Fig. S8. Shallow remineralization depths produce the best model fit to Paleozoic I/Ca distributions regardless of atmospheric pCO_2 levels (Fig. 4).

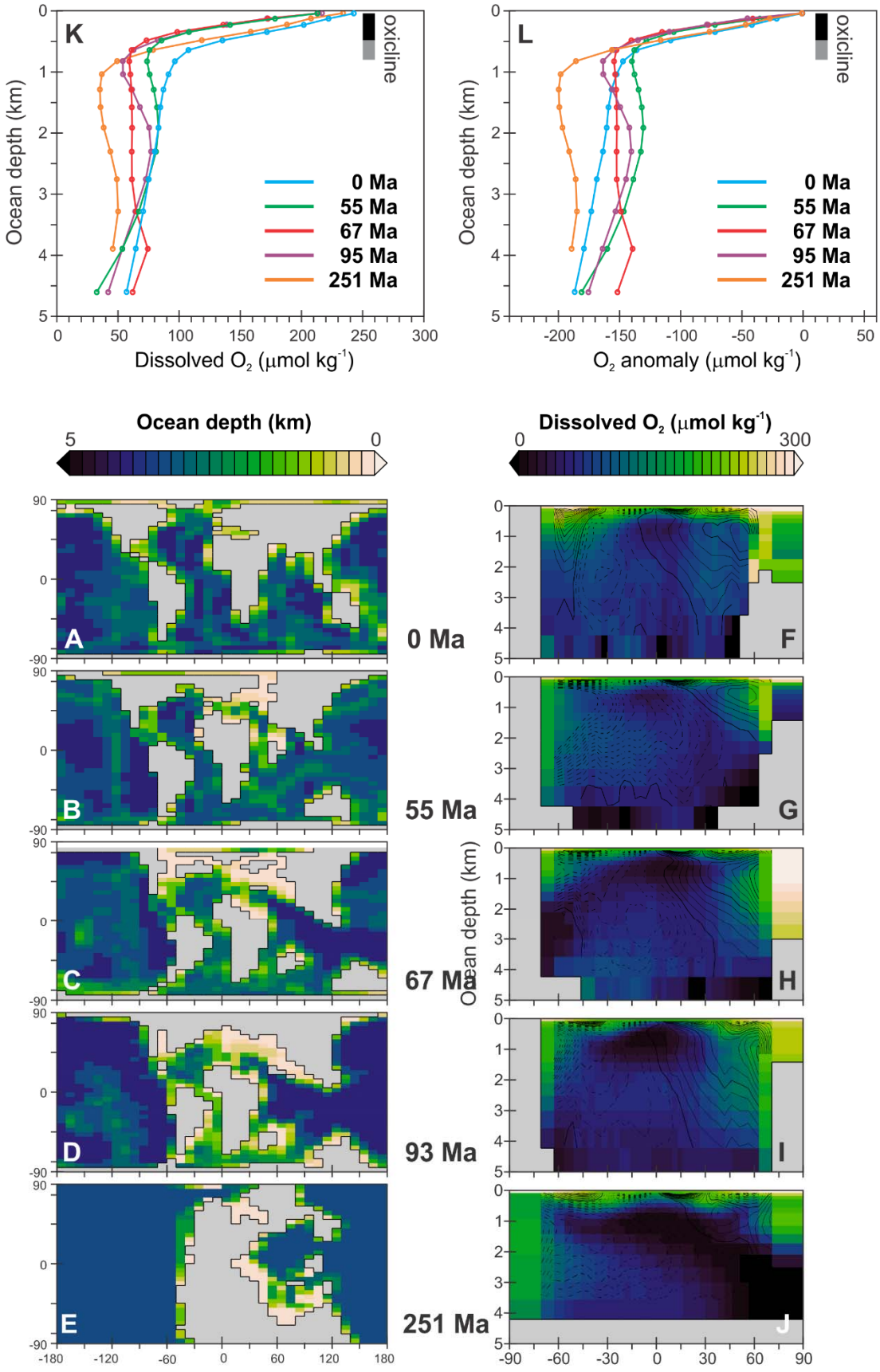
K
L
oxicline
Ocean depth (km)
Dissolved O2 (μmol kg-1)
O2 anomaly (μmol kg-1)
0 Ma
55 Ma
67 Ma
95 Ma
251 Ma
Ocean depth (km)
Dissolved O2 (μmol kg-1)
A
B
C
D
E
F
G
H
I
J
0 Ma
55 Ma
67 Ma
93 Ma
251 Ma

Fig. S9. Model-based analysis of the influence of changing continental configuration and climate on the oxycline. Panels A-E are the continental configurations and bathymetry for the 5 experiments. F-J show the zonal mean distribution of dissolved oxygen in the ocean, overlain for illustration with the global overturning stream-function (solid contours representing positive, clockwise overturning circulation, and dashed contours anticlockwise circulation). Panels K and L summarize the global mean distribution of dissolved oxygen, as absolute values (K) and anomalies (L) relative to mean modern surface dissolved oxygen concentrations in the model.

We used a suit of previously published continental and climate configurations for modern and the past (*29, 37*), the late Paleocene/early Eocene (55 Ma) (*47*), the end Cretaceous (67 Ma) (*48*), the mid Cretaceous (97 Ma) (*49*), and the late Permian (251 Ma) (*28*). These configurations encompass continental configurations ranging from the Pangea supercontinent (late Permian) to highly dispersed (modern), atmospheric CO_2 varying from 278 ppm (modern) through 2,800 ppm (late Permian), and sea level stand from low (modern and late Permian) to high (mid Cretaceous). We hence are testing a reasonably full range of potential states of ocean circulation. In order to remove effects of changing atmospheric oxygen and organic matter remineralization (the two key controls we explore in the paper in order to explain the I/Ca data), we keep atmospheric O_2 fixed in the model at modern concentrations, and the remineralization depth of organic matter fixed and according to the modern calibration in cGENIE (*37*). In addition, we employ a surface ocean PO_4-restoring scheme in which organic matter export is diagnosed according to a relaxing of surface ocean PO_4 concentrations towards zero. We do this in order to achieve an approximately constant global export of organic matter across all the experiments (and indeed find that the range is relatively restricted – ranging from 8.8 PgC yr^{-1} (0 Ma) to 10.0 PgC yr^{-1} (251 Ma)). Hence, across all the modern configurations the total ocean oxygen consumption will be approximately equal and the only fact that can significantly influence the shape of the oxycline is ocean circulation and mixing. We run all experiments for 10 kyr to steady state. It can be seen that the slope of dissolved oxygen against depth – the steepness of the oxycline, is approximately invariant across all configurations (panels K, L). The only minor differences are in the apparent depth of the base of the oxycline, with the configuration from 251 Ma showing a very slightly deeper (no more than a few 100 m) point at which the rate of decline of dissolved oxygen with depth starts to flatten out. From this we conclude that on a global scale, the only factors that would substantially affect the slope and/or depth of the oxycline through time will be the organic carbon remineralization depth (*28*) and atmospheric oxygen.

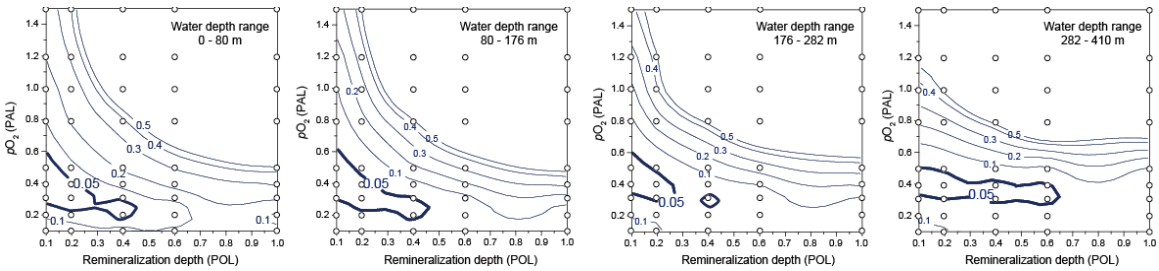

Fig. S10. [IO_3^-] distributions in the top four layers of ocean waters in cGENIE compared with Paleozoic I/Ca distributions, showing similar RSS patterns.

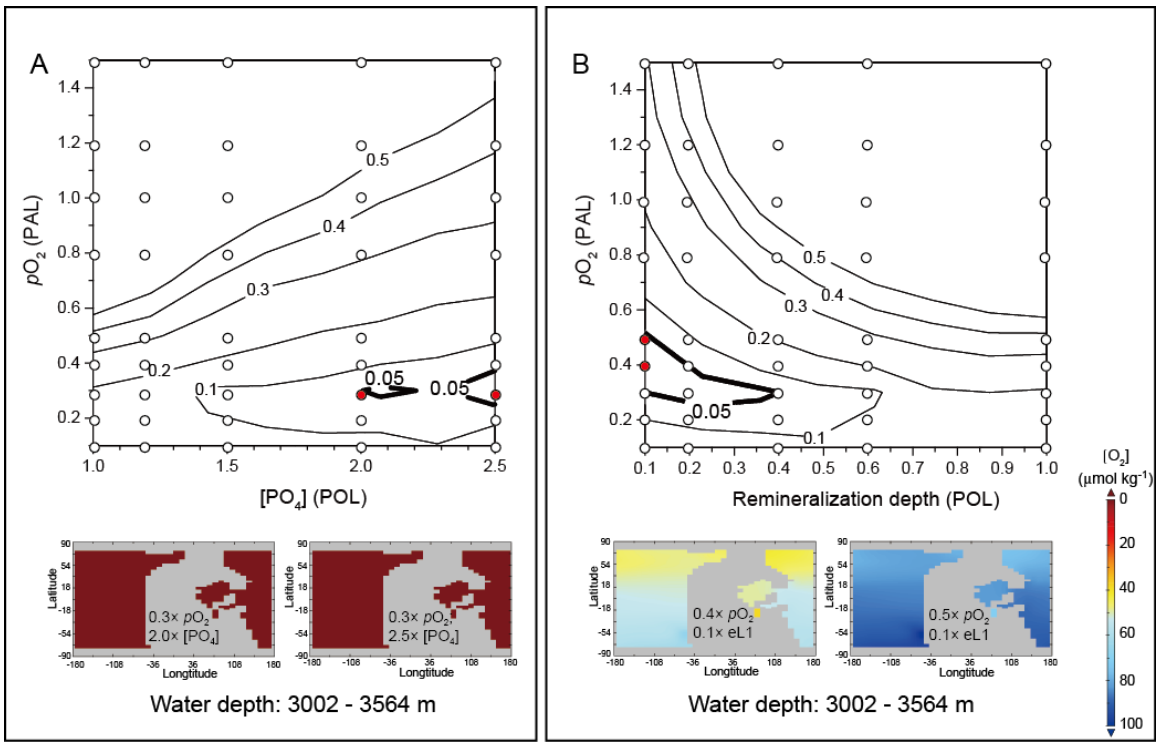

Fig. S11. A. High phosphate concentrations in seawater required to produce low RSS would result in widespread anoxia in deep oceans. Two red dots in RSS contours mark the pO_2 and $[PO_4]$ settings corresponding to the two deep-ocean $[O_2]$ maps below. **B.** shallow remineralization depth produces good data–model fit and well-oxygenated deep oceans. In addition to remineralization depths, $[IO_3^-]$ distributions can be affected by the ocean PO_4 inventory, which influences productivity and oxygen consumption in subsurface waters. Increasing $[PO_4]$ in seawater up to 2.5 POL reduces RSS values, but triggers anoxia in the deep ocean, which is inconsistent with generally stable $\delta^{98}Mo$ values since 400 Ma (*50*). By contrast, model runs with shallow remineralization depths can produce a similar range of RSS values while maintaining oxygenated deep-ocean conditions. Furthermore, there is no independent proxy evidence for a step-wise decrease in seawater $[PO_4]$ at ~200 Ma to account for the observed I/Ca increase.

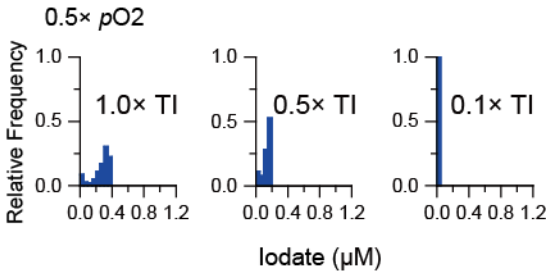

Fig. S12. Surface-ocean iodate IO_3^- distributions with decreasing ocean iodine inventory. These frequency distributions do not reproduce the lognormal type of distribution as observed in Paleozoic I/Ca data. Modern fluxes of iodine input and output from seawaters may be orders of magnitude lower than that of iodine recycling in the water column (*7*). IO_3^- (instead of I^-) sorption on organic matter at the sediment-water interface is a major sink of iodine, which appears to be stabilized by a negative feedback between the amount of organic matter as a substrate on the seafloor and bottom-water oxygenation preventing IO_3^- reduction (*51*). No evidence supports either global organic matter burial rate or bottom water [O_2] level mimicking the I/Ca record. Therefore, secular changes in total iodine concentration are also unlikely to dominate the trends observed in our I/Ca record.

Additional Data table S1 (separate file).
Summary of samples and materials.

Additional Data table S2 (separate file).
Phanerozoic I/Ca data

REFERENCES AND NOTES

1. A. H. Knoll, *Cold Spring Harbor Perspectives in Biology* **6**, (2014).
2. R. F. Keeling, A. Kortzinger, N. Gruber, *Annual Review of Marine Science* **2**, 199-229 (2010).
3. T. W. Lyons, C. T. Reinhard, N. J. Planavsky, *Nature* **506**, 307-315 (2014).
4. T. W. Dahl *et al.*, *PNAS* **107**, 17911-17915 (2010).
5. E. A. Sperling *et al.*, *Nature* **523**, 451-454 (2015).
6. Z. Lu *et al.*, *Nature Communications* **7:11146**, (2016).
7. Z. Lu, H. C. Jenkyns, R. E. M. Rickaby, *Geology* **38**, 1107–1110 (2010).
8. G. W. Luther, T. Campbell, *Deep-Sea Research Part A-Oceanographic Research Papers* **38**, S875-S882 (1991).
9. E. L. Rue, G. J. Smith, G. A. Cutter, K. W. Bruland, *Deep-Sea Research Part I-Oceanographic Research Papers* **44**, 113-134 (1997).
10. J. Podder *et al.*, *Geochim. Cosmochim. Acta* **198**, 218-228 (2017).
11. D. S. Hardisty *et al.*, *Earth Planet. Sci. Lett.* **463**, 159-170 (2017).
12. D. S. Hardisty *et al.*, *Geology*, (2014).
13. X. Zhou *et al.*, *Paleoceanography* **30**, 510-526 (2015).
14. X. L. Zhou, E. Thomas, R. E. M. Rickaby, A. M. E. Winguth, Z. L. Lu, *Paleoceanography* **29**, 964-975 (2014).
15. W. Lu *et al.*, *Geochemical Perspectives Letters* **5**, 53-57 (2017).
16. C. T. Edwards, D. A. Fike, M. R. Saltzman, W. Lu, Z. Lu, *Earth Planet. Sci. Lett.* **481**, 125-135 (2018).
17. G. R. Loope, L. R. Kump, M. A. Arthur, *Chem. Geol.* **351**, 195-208 (2013).
18. R. Chance, A. R. Baker, L. Carpenter, T. D. Jickells, *Environmental Science-Processes & Impacts* **16**, 1841-1859 (2014).
19. T. M. Lenton *et al.*, *Proceedings of the National Academy of Sciences* **113**, 9704-9709 (2016).
20. I. J. Glasspool, A. C. Scott, *Nat. Geosci.* **3**, 627-630 (2010).
21. R. A. Berner, *Geochim. Cosmochim. Acta* **70**, 5653-5664 (2006).
22. N. M. Bergman, T. M. Lenton, A. J. Watson, *Am. J. Sci.* **304**, 397-437 (2004).
23. T. M. Lenton, S. J. Dainesa, B. J. Mills, *Earth Sci Rev* **178**, 1-28 (2018).
24. P. G. Falkowski *et al.*, *Science* **309**, 2202-2204 (2005).
25. L. R. Kump, *Nature* **335**, 152-154 (1988).
26. T. J. Algeo, R. A. Berner, J. B. Maynard, S. E. Scheckler, *GSA Today* **5**, 64–66 (1995).
27. H. D. Holland, *Philosophical Transactions of the Royal Society B-Biological Sciences* **361**, 903-915 (2006).
28. K. M. Meyer, A. Ridgwell, J. L. Payne, *Geobiology* **14**, 207-219 (2016).
29. A. Ridgwell *et al.*, *Biogeosciences* **4**, 87-104 (2007).
30. M. E. Katz, Z. V. Finkel, D. Grzebyk, A. H. Knoll, P. G. Falkowski, *Annual Review of Ecology Evolution and Systematics* **35**, 523-556 (2004).
31. R. E. Martin, *Global Planet. Change* **11**, 1-23 (1995).
32. P. G. Falkowski *et al.*, *Science* **305**, 354-360 (2004).
33. N. J. Butterfield, *Geobiology* **7**, 1-7 (2009).
34. G. A. Logan, J. M. Hayes, G. B. Hieshima, R. E. Summons, *Nature* **376**, 53-56 (1995).

35. J. L. Payne *et al.*, *Photosynth. Res.* **107**, 37-57 (2011).
36. N. A. Heim, M. L. Knope, E. K. Schaal, S. C. Wang, J. L. Payne, *Science* **347**, 867-870 (2015).
37. L. Cao *et al.*, *Biogeosciences* **6**, 375-390 (2009).
38. A. Tagliabue *et al.*, *Global Biogeochem. Cycles* **30**, 149-174 (2016).
39. H. Elderfield, V. W. Truesdale, *Earth Planet. Sci. Lett.* **50**, 105-114 (1980).
40. S. K. Lyons *et al.*, *Nature* **529**, 80-U183 (2016).
41. L. A. Hardie, *Geology* **31**, 785-788 (2003).
42. J. Farkas *et al.*, *Geochim. Cosmochim. Acta* **71**, 5117-5134 (2007).
43. A. Ridgwell, *Mar. Geol.* **217**, 339-357 (2005).
44. T. K. Lowenstein, L. A. Hardie, M. N. Timofeeff, R. V. Demicco, *Geology* **31**, 857-860 (2003).
45. R. A. Berner, *Am. J. Sci.* **304**, 438-453 (2004).
46. L. A. Hardie, *Geology* **24**, 279-283 (1996).
47. A. Ridgwell, D. N. Schmidt, *Nat. Geosci.* **3**, 196-200 (2010).
48. A. Schmidt *et al.*, *Nat. Geosci.* **9**, 77-+ (2016).
49. F. M. Monteiro, R. D. Pancost, A. Ridgwell, Y. Donnadieu, *Paleoceanography* **27**, (2012).
50. B. Kendall *et al.*, *Geochim. Cosmochim. Acta* **156**, 173-193 (2015).
51. X. Zhou *et al.*, *Chem. Geol.* **457**, 95-106 (2017).